Hybrid Local-global Power-sharing Scheme for Droop-free Controlled Microgrids

Kunyu Zuo, *Member*, *IEEE*, and Lei Wu, *Fellow*, *IEEE*

***Abstract*—The droop-free control adopted in microgrids has been designed to cope with global power-sharing goals, i. e., sharing disturbance mitigation among all controllable assets to even their burden. However, limited by neighboring communication, the time-consuming peer-to-peer coordination of the droop-free control slows down the nodal convergence to global consensus, reducing the power-sharing efficiency as the number of nodes increases. To this end, this paper first proposes a local power-sharing droop-free control scheme to contain disturbances within nearby nodes, in order to reduce the number of nodes involved in the coordination and accelerate the convergence speed. A hybrid local-global power-sharing scheme is then put forward to leverage the merits of both schemes, which also enables the autonomous switching between local and global power-sharing modes according to the system states. Systematic guidance for key control parameter designs is derived via the optimal control methods, by optimizing the power-sharing distributions at the steady-state consensus as well as along the dynamic trajectory to consensus. System stability of the hybrid scheme is proved by the eigenvalue analysis and Lyapunov direct method. Moreover, simulation results validate that the proposed hybrid local-global power-sharing scheme performs stably against disturbances and achieves the expected control performance in local and global power-sharing modes as well as mode transitions. Moreover, compared with the classical global power-sharing scheme, the proposed scheme presents promising benefits in convergence speed and scalability.**

***Index Terms*—Droop-free control, local power-sharing, optimal control, Lyapunov stability.**

NOMENCLATURE

A. Matrices, Vectors, and Sets

$\Delta \boldsymbol{p}^{\bar{b},i}$	Adjustments of battery storage system (BSS) against disturbance i
$\Delta \boldsymbol{p}^{n,i}$	Adjustments of net power against disturbance i
$\Delta \boldsymbol{p}^{c,i}$	Adjustments of power compensation against disturbance i
$\Delta \boldsymbol{p}^{d,i}$	Net load of disturbance i
$\boldsymbol{\omega}$, $\boldsymbol{\theta}$	Vectors of nodal frequencies and phase angles
$\boldsymbol{A}$	Adjacency matrix of communication network
$\boldsymbol{B}$	Susceptance matrix of electrical network
$\boldsymbol{D}_p$	Normalization matrix of BSS capacities
$\boldsymbol{E}$	Matrix of anti-windup control gains
$\boldsymbol{H}$	Matrix of droop-free control gains
$\boldsymbol{I}$	Identity matrix
$\boldsymbol{K}$	Matrix of compensation control gains
$\boldsymbol{L}_A$	Laplacian matrix of adjacency matrix $\boldsymbol{A}$
$\mathcal{N}$, $\mathcal{E}$	Sets of nodes and electrical lines
$\boldsymbol{p}^b$, $\boldsymbol{p}^d$, $\boldsymbol{p}^n$	Vectors of BSS power, demands, and net power
$\boldsymbol{p}^{\bar{b}}$	Vector of normalized BSS power
$\boldsymbol{p}^c$	Vector of power compensations
$\boldsymbol{p}^p$	Vector of relative power positions
$\mathcal{U}$, $\mathcal{S}$	Unsaturated and saturated BSSs
$\mathcal{W}$	Positive definite matrix

B. Indices, Functions, and Modules

$dzn(\cdot)$	Dead-zone module
i, j	Indices of nodes
$\mathcal{J}^{\mathrm{I}}$	Objective in steady-state power distribution
$\mathcal{J}^{\mathrm{II}}$	Objective in dynamic performance
L^g	Lyapunov energy function in global mode
L^a	Lyapunov energy function in autonomous mode transition
$sat(\cdot)$	Saturator module
$\mathrm{sgn}(\cdot)$	Sign module
$\dot{(\cdot)}$	Time derivative
$\lvert\cdot\rvert$	Cardinality
$(\cdot)^*$, $(\cdot)^{*-}$	Steady state and last steady state
$\overline{(\cdot)}$	Distance to steady state
$\Delta(\cdot)$	Adjustment between two steady states

C. Parameters

ρ^{I}	Power distribution weight
ρ^{II}	Dynamic performance weight
$A_{(i,j)}$	Communication between node i and j
$b_{(i,j)}$	Susceptance between node i and j
e	Anti-windup control gain
h	Droop-free control gain
k	Compensation control gain

Manuscript received: September 10, 2023; revised: December 18, 2023; accepted: March 28, 2024. Date of CrossCheck: March 28, 2024. Date of online publication: April 18, 2024.

This work was supported in part by the PSEG Foundation gift.

K. Zuo and L. Wu (corresponding author) are with Electrical and Computer Engineering Department, Stevens Institute of Technology, Hoboken, NJ 07030, USA (e-mail: kzuo@stevens.edu; lei.wu@stevens.edu).

DOI: 10.35833/MPCE.2023.000652

N	Number of nodes
$p_i^{b,nominal}$	Nominal power of BSS at node i

D. Variables

λ_i^g	The i^{th} eigenvalue in global design
$\omega_i(t)$	Frequency at node i
$H_{(i,i)}$	Droop-free control gain at node i
$K_{(i,i)}$	Compensation control gain at node i
$p_i^b(t)$	Normalized BSS power at node i
$p_i^d(t)$	Nodal demand at node i
$p_i^p(t)$	Relative power position of node i to neighbors
$p_i^c(t)$	Power composition at node i
r	Ratio of droop-free control gain to compensation control gain

I. Introduction

PROGRESSING towards a carbon-free power system, recent government policies [1], [2] have specified the minimum renewable energy penetration requirements in the coming years, promoting the integration of distributed energy resources (DERs) such as renewable energy sources and energy storage systems in the distribution sector. With the increasing penetration of variable and uncertain renewable energy in the distribution sector, it becomes practically important to form DERs into renewable-centric microgrids that can maintain normal operations in the islanded mode and/or provide steady power exchanges with the main grid in the grid-connected mode. To this end, the primary control layer, which manages power balance, power-sharing, and synchronization [3], needs to be upgraded to accommodate the emerging need for such renewable-centric microgrids.

Currently, renewable-centric microgrids usually adopt droop control as the primary control layer [4], [5], which is derived from the droop characteristics in power systems. That is, voltage-sourced inverters (VSIs) rely on controllable DERs on the DC side, battery storage systems (BSSs) in particular, to immediately balance net load disturbances and droop the nodal frequency to share the disturbance burden.

Droop control is a communication-free decentralized control framework [6]. Since power states are not broadcasted in the droop-based primary control layer, for microgrids with mismatched line impedance [7], such decentralized coordination will lead to steady-state errors in active, reactive, and harmonic power-sharing [8] - [10], and even stability issues [11]. Besides, droop controllers coordinated via frequency deviation signals would inevitably cause frequency issues such as significant noises [12] and system-wide frequency drops [13].

Droop-free control, as a neighboring communication-based distributed control, draws increasing attention to resolving the above issues [14], [15]. Benefiting from directly exchanging the nodal power information with neighbors, droop-free control can accurately coordinate power-sharing in active, reactive, harmonic, and imbalanced power [16], [17]. Moreover, using the distributed averaging-based integral control method in coordination [18], the system frequency (i.e., the average of nodal frequencies) during the control process can be kept around the nominal value to avoid system frequency drop in primary control.

Existing studies on primary control exclusively focus on global power-sharing strategies. That is, for a disturbance of any size and at any location in microgrids, all BSSs collectively respond to reach the global consensus.

Typically, global power-sharing can be realized by setting identical primary control gains and weights for power signals [19], ensuring that the disturbances are equally shared among BSSs in microgrids. However, such a method fails to leverage heterogeneous capacities and configurations of BSSs. To address this limitation, nodal power signals are normalized with respect to their distinct capacities [20], allowing disturbances to be proportionally shared among BSSs according to their capabilities. Alternatively, nodal power signals are additionally processed through an incremental cost function [21], facilitating BSSs pursuing global economic sharing.

In addition, advanced control methods are introduced to improve global power-sharing. Adaptive control is employed in [22] to dynamically modify control gains based on the price changes, enabling the primary controller to track the minimum global cost. Model predictive control is used in primary control to minimize the error function, enabling the outputs of VSIs to closely follow the power-sharing reference [23]. A sliding-mode control is proposed in [24] to improve the droop-free robustness against potential clock drifts in the sparse communication network. Data-driven controller is constructed in [25] to minimize system-wide sensitivity to noises, resulting in more robust and stable transients during power-sharing.

The above power-sharing designs invoke all BSSs to average the sharing burden and pursue a global consensus, even for disturbances of moderate magnitudes that can be appropriately mitigated by onsite BSSs. It causes a main issue for droop-free control: it is time-consuming to reach a global consensus because of the sparse neighboring communication [26], and the microgrid will long-lasting operate in a transient process.

To address the issues, a local power-sharing design of droop-free control is proposed in the paper that can properly retain disturbances in a small region depending on BSS capacities and system operation conditions, speeding up the coordination and avoiding overly frequent switch on charging or discharging status of BSSs.

In the proposed local power-sharing design, power-sharing request is discounted at each propagation step of the neighboring communication, gradually reducing the compensation responsibility as the number of propagation steps increases. That is, the power-sharing consensus is formed unevenly, and BSSs closer to a local disturbance will undertake more power-sharing burden. In this manner, the droop-free control process depends on both the location and size of disturbances: for light disturbances, it would involve a few nearby nodes only; as disturbances increase, the coordination region will automatically expand. That is, the local power-sharing design for droop-free control can effectively contain the im-

pact of disturbances within a proper region, simplifying the coordination process and accelerating convergence.

The proposed local power-sharing droop-free control scheme is further extended to a hybrid local-global power-sharing scheme to address the operational limits of BSSs via the anti-windup feedback controller [27]. Specifically, the anti-windup feedback control provides a continuous process to smooth the state space switch, by holding control variables on the boundaries and releasing them once the variables tend to recover [28]. Thus, when heavy disturbances cause certain BSSs to reach their power limits, the proposed hybrid local-global power-sharing scheme can autonomously and smoothly switch to the global power-sharing mode, enabling the power-sharing burden promptly allocated to other BSSs. Moreover, the system can autonomously and smoothly transit back to the local power-sharing mode once the boundary limits become inactive. Hence, the proposed hybrid scheme preserves the benefits of both local and global power-sharing strategies.

In addition, the system stability of the proposed hybrid scheme is deduced via eigenvalue analysis [19] and Lyapunov direct methods [29]. On this basis, systematic guidance on the design of control gains is derived via the optimal control methods [30], by optimizing the power-sharing distributions at the steady-state consensus as well as along the dynamic trajectory to consensus. The proposed design is further quantitatively compared with the global power-sharing droop-free control [15] via simulation studies, showing its advantages in terms of power-sharing burden, convergence speed, and scalability.

The main contributions of the paper are described as follows.

1) Local power-sharing consensus for droop-free control is optimized to effectively contain the impact of disturbances within a proper region, simplifying the coordination process and accelerating the convergence.

2) The proposed hybrid scheme, by taking advantage of both local and global power-sharing consensus, enables microgrids to autonomously switch between the two modes according to the operation status of the microgrid.

3) System stability is proved by eigenvalue analysis and Lyapunov direct methods. Systematic guidance on the design of control gains is further derived via optimal control methods.

The remainder of the paper is organized as follows. Section II presents the proposed hybrid local-global power-sharing scheme for droop-free controlled microgrids. Section III proves the system stability and derives systematic guidance on the optimal design of control gains. Case studies are presented in Section IV to validate the proposed hybrid scheme and compare its performance against the droop-free control. Section V concludes this paper.

II. Hybrid Local-global Power-sharing Scheme

This section presents the expected performance of the proposed hybrid scheme for droop-free controlled microgrids, followed by the detailed design of the hybrid controller. Specifically, the local power-sharing droop-free control scheme is first presented to speed up convergence by only involving a limited number of neighboring nodes in the coordination process. A global power-sharing mode is further discussed to handle the operational limits of BSSs via the anti-windup feedback controller. Finally, the hybrid scheme that can operate at each of the local and global power-sharing modes and smoothly switch between the two modes is proposed for accommodating various operation conditions.

A. Expected Performance of Proposed Hybrid Scheme

We take the discharging operation of BSSs for the detailed discussion, while the charging operation shares a similar set of operation limits [31] and can be analyzed analogously. Both the discharging and charging operations of BSSs are covered in the proposed controller design.

As shown by the red dotted lines in Fig. 1, three discharging power limits of BSSs are defined, including nominal power, rated power, and peak power.

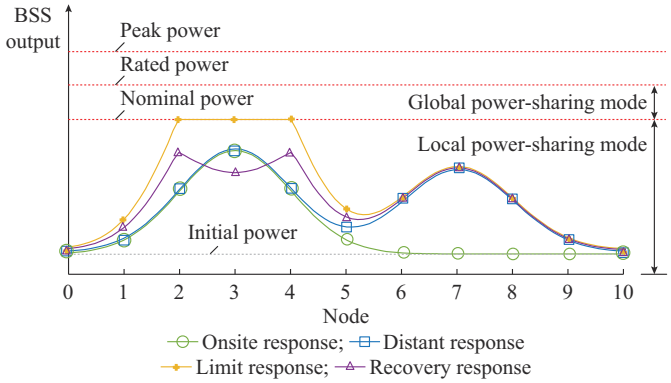

Fig. 1. Power distribution in hybrid local-global power-sharing scheme.

1) Nominal power: BSSs are recommended to routinely operate below the nominal power for high energy efficiency and less battery degeneration [32].

2) Rated power: BSSs can continuously and safely operate between nominal power and rated power, but with lower efficiency. Due to the characteristics of battery units [33], [34], the efficiency loss in this zone will grow exponentially with respect to the power output level.

3) Peak power: BSSs can only operate between rated power and peak power for a very short period [35] such as 5-15 s. It promotes BSSs to act as voltage sources for holding large disturbances for a short period.

Based on the characteristics of the three discharging power levels, the expected performance of the proposed hybrid scheme is described as follows.

1) BSS discharging power shall never exceed the peak power, and shall return below the rated power as quickly as possible.

2) Within the lower-efficiency discharging power range (i.e., between the nominal power and rated power), the system shall operate in the global power-sharing mode to share the burden among BSSs for reducing efficiency loss.

3) Within the discharging power range of the nominal power, the system shall operate in the local power-sharing mode to contain the impact of disturbances within a proper

region, simplify the coordination process, and accelerate convergence. Specifically, the local power-sharing mode involves four typical response actions including onsite response, distant response, limit response, and recovery response, as demonstrated in Fig. 1.

① Onsite response refers to that a disturbance can be adequately mitigated by nearby nodes. For instance, in response to a disturbance at node 3, the power-sharing is moved from the gray dotted line to the green solid line, indicating that the disturbance is mainly balanced by node 3 and its two nearest neighboring nodes 2 and 4.

② Distant response refers to that a disturbance will introduce minimal effects on remote nodes. For instance, when the system operates at the green solid line, a new disturbance at node 7 alters the nodal power-sharing to the blue solid line. It shows that the majority of disturbances are taken by the nearby nodes 5-9, while the changes in power-sharing of remote nodes 0-4 are negligible.

③ Limit response refers to that if the onsite BSS reaches its nominal power and the BSSs of other nodes remain below their nominal power levels, more nearby nodes will get involved in the local power-sharing process gradually to the efficiency goal. For instance, the orange solid line shows that after another disturbance at node 3, BSSs at nearby nodes 2-4 reach their nominal power, and further nodes (e.g., nodes 1 and 5) will be more engaged in mitigating the disturbance.

④ Recovery response refers to that when BSSs reduce their discharging power levels against negative disturbances, they shall follow the same local power-sharing principles discussed above, i.e., closer BSSs will take a larger portion of negative disturbances, as shown in the purple solid line.

4) The hybrid control shall autonomously switch between the two modes based on the dynamic system operation status (i.e., below or above the nominal power).

In summary, the proposed hybrid scheme shall enable microgrids to properly operate at each of the local and global power-sharing modes and to smoothly switch between the two, following the expected performance described above.

It is noteworthy that microgrid control usually includes: ① primary control which acts promptly against instant disturbances to maintain power balance, synchronization, and power-sharing [7]; ② secondary control which is triggered every few seconds to regulate frequency and voltage back to the nominal values [36]; and ③ tertiary control which is activated every few minutes to provide economic operation points for DERs [37]. The state of charge (SOC) management is usually associated with the tertiary control layer [38]. For the fast primary control discussed in this paper that works in a finer time granularity, SOC management is not included in this process.

B. Design of Hybrid Controller

To achieve the expected control performance, a hybrid local-global power-sharing scheme is proposed on the foundation of the classical global power-sharing scheme, as shown in Fig. 2, where SPWM stands for sinusoidal pulse width modulation. The blue control loop is the classical global power-sharing droop-free control for active power [17]-[19]. Specifically, the active power flow can be calculated as in (1a). The line susceptance matrix of the electrical network $\boldsymbol{B}$ is given in (1b), where $b_{(i,j)}$ is the susceptance of the electrical line $(i,j) \in \mathcal{E}$ and $b_{(i,j)}=0$ for $(i,j) \notin \mathcal{E}$.

$$\boldsymbol{p}^b+\boldsymbol{p}^d=\boldsymbol{p}^n=\boldsymbol{B}\boldsymbol{\theta} \tag{1a}$$

$$\boldsymbol{B}=\begin{bmatrix} \sum_{j\in\mathcal{N},j\neq 1} b_{(1,j)} & -b_{(1,2)} & \cdots & -b_{(1,N)} \\ -b_{(2,1)} & \sum_{j\in\mathcal{N},j\neq 2} b_{(N,j)} & \cdots & -b_{(2,N)} \\ \vdots & \vdots & & \vdots \\ -b_{(N,1)} & -b_{(N,2)} & \cdots & \sum_{j\in\mathcal{N},j\neq N} b_{(N,j)} \end{bmatrix} \tag{1b}$$

$$\dot{\boldsymbol{\theta}}=\boldsymbol{\omega} \tag{1c}$$

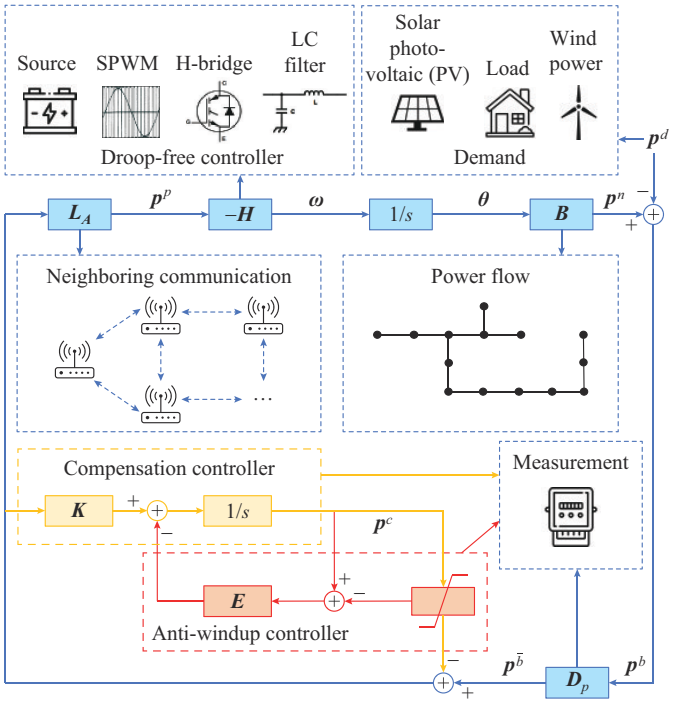

Fig. 2. Block diagram of hybrid local-global power-sharing scheme.

The dynamic operation states are normalized as in (2a), where $\boldsymbol{D}_p$ is formed as in (2b). It scales the discharging/charging power output of the i^{th} BSS into the range of $[-1, 1]$ when BSS operates within the nominal power $p_i^{b,nominal}$. The normalized BSS states will be broadcasted to nearby nodes through the neighboring communication network.

$$\boldsymbol{p}^{\bar{b}}=\boldsymbol{D}_p\boldsymbol{p}^b \tag{2a}$$

$$D_p(i,i)=1/p_i^{b,nominal} \quad i\in\mathcal{N} \tag{2b}$$

The relative power position $\boldsymbol{p}^p$ is calculated by comparing the neighbors' normalized power levels as in (3a), where $A_{(i,j)}=A_{(j,i)}=1$ if BSSs i and j directly communicate with each other, and $A_{(i,j)}=0$ otherwise. Hereby, $\boldsymbol{p}^p$ can depict the relative output state of a BSS compared with its neighbors. The information is consequently fed back with the classical

droop-free controller [17] - [20] as in (3b), where $\boldsymbol{H}=h\boldsymbol{I}$. With this, the droop-free controller can decrease (increase) the nodal frequencies $\boldsymbol{\omega}$ to release (undertake) power burden to (from) neighboring BSSs, until all the normalized outputs converge to a consensus and $\boldsymbol{p}^p=\boldsymbol{0}$.

$$p_i^p(t)=\sum_{j\in\mathcal{N},j\neq i}A_{(i,j)}\left(p_i^{\bar{b}}(t)-p_j^{\bar{b}}(t)\right)\quad i\in\mathcal{N} \tag{3a}$$

$$\omega_i(t)=-H_{(i,i)}p_i^p(t)\quad i\in\mathcal{N} \tag{3b}$$

Equations (3a) and (3b) can be organized in a matrix form as in (4). Since the column sum of Laplacian matrix $\boldsymbol{L}_A$ is equal to 0, the system frequency (i.e., the average value of nodal frequencies $\boldsymbol{\omega}$) stays at 0 during the droop-free dynamic process. It is noteworthy that faster control dynamics such as the inner voltage and current loops are assumed to be well-tuned. Moreover, as they are much faster than the primary control, their dynamics are not included in the droop-free controller dynamic equations.

$$\boldsymbol{\omega}=-h\boldsymbol{L}_A\boldsymbol{p}^{\bar{b}} \tag{4}$$

By combining (1), (2), and (4), the state-space equation of the global power-sharing droop-free controlled microgrid can be formulated as in (5), illustrated as the blue control loop in Fig. 2. With the proper setting of the control gain h, the system will converge to the global power-sharing, i. e., $p_i^{\bar{b}}(t)=p_j^{\bar{b}}(t)$ for $\forall i,j\in\mathcal{N}$. The equilibrium point is presented as in (6), indicating the relative power positions among the neighboring BSSs are zeros, where $\boldsymbol{0}_N$ is a zero vector of size N.

$$\dot{\boldsymbol{p}}^n=-h\boldsymbol{B}\boldsymbol{L}_A\boldsymbol{D}_p\left(\boldsymbol{p}^n-\boldsymbol{p}^d\right) \tag{5}$$

$$\boldsymbol{0}_N=\boldsymbol{L}_A\boldsymbol{p}^{\bar{b}*}=\boldsymbol{L}_A\boldsymbol{D}_p\left(\boldsymbol{p}^{n*}-\boldsymbol{p}^{d*}\right) \tag{6}$$

The proposed local power-sharing droop-free control scheme embeds an additional compensation controller and an anti-windup controller into the global power-sharing droop-free control loop, respectively, which are shown as the yellow and red blocks in Fig. 2, respectively.

The compensation controller records the compensation signal that can depict the location and magnitude of disturbances balanced by the BSS. Specifically, once a disturbance occurs, the difference between the BSS power and the compensated reference is calculated as the balanced disturbances. With this, the corresponding compensation controller begins to accumulate the power compensation $\boldsymbol{p}^c$ based on balanced disturbances. The information containing location and magnitude is fed back to the BSS measurement $\boldsymbol{p}^{\bar{b}}$ to discount the BSS power. To this end, the power broadcasted in the neighboring communication network is modified from the normalized power $\boldsymbol{p}^{\bar{b}}$ to $\boldsymbol{p}^{\bar{b}}-\boldsymbol{p}^c$, changing the equilibrium point from (6) to (7). Consequently, the power distribution can be formed unevenly since the stabilized BSS output $p_i^{\bar{b}*}(t)$ is based on the local composition $p_i^{c*}(t)$.

$$\boldsymbol{0}_N=\boldsymbol{L}_A\left(\boldsymbol{p}^{\bar{b}*}-\boldsymbol{p}^{c*}\right) \tag{7}$$

The local compensation process can effectively operate under unconstrained conditions. However, if $\boldsymbol{p}^c$ of a local compensation controller exceeds the nominal power, it would drive the output of this BSS above the nominal power, while the outputs of other BSSs could still stay below their nominal power levels, violating the expected control performance of limit response.

To this end, the anti-windup controller (red block in Fig. 2) consisting of a saturator and a feedback controller is further included. Once the accumulated local power compensation reaches the nominal power, the saturator smoothly fixes the output at the boundary to retain the BSS in the zone of high operational efficiency. With this, the equilibrium point is further modified to (8). In addition, the anti-windup feedback loop is adopted to counteract the growth of the compensation process and lock the integral value $\boldsymbol{p}^{c*}$ on the boundary of the saturator. Otherwise, the continually accumulated value at the integrator could form a surplus buffer, impacting the performance of the recovery response and local power-sharing.

$$\boldsymbol{0}_N=\boldsymbol{L}_A\left(\boldsymbol{p}^{\bar{b}*}-sat\left(\boldsymbol{p}^{c*}\right)\right) \tag{8}$$

Therefore, the proposed local power-sharing droop-free control scheme can serve the four response actions described in Fig. 1. The formulation of the compensation controller and anti-windup controller can be organized as in (9a), where the normalized BSS output $\boldsymbol{p}^{\bar{b}}$, trimmed compensation power $sat\left(\boldsymbol{p}^c\right)$, and anti-windup feedback $dzn\left(\boldsymbol{p}^c\right)$ together act on the integral process of $\boldsymbol{p}^c$; $sat\left(\boldsymbol{p}^c\right)$ is formulated as in (9b), such that $sat\left(p_i^c(t)\right)=p_i^c(t)$ if $-1\le p_i^c(t)\le 1$ for $\forall i\in\mathcal{N}$; otherwise, $sat\left(p_i^c(t)\right)=-1$ or 1 depending on the sign of $p_i^c(t)$. $\boldsymbol{E}=e\boldsymbol{I}$ is the anti-windup control gain, and $dzn\left(\boldsymbol{p}^c\right)$ is modeled as in (9c) such that the anti-windup feedback is activated when $sat\left(p_i^c(t)\right)\neq p_i^c(t)$ for $\forall i\in\mathcal{N}$.

$$\dot{\boldsymbol{p}}^c=\boldsymbol{K}\left(\boldsymbol{p}^{\bar{b}}-sat\left(\boldsymbol{p}^c\right)\right)-\boldsymbol{E}\cdot dzn\left(\boldsymbol{p}^c\right) \tag{9a}$$

$$sat\left(\boldsymbol{p}^c\right)=\mathrm{sgn}\left(\boldsymbol{p}^c\right)\cdot\min\left(\left|\boldsymbol{p}^c\right|,1\right) \tag{9b}$$

$$dzn\left(\boldsymbol{p}^c\right)=\boldsymbol{p}^c-sat\left(\boldsymbol{p}^c\right) \tag{9c}$$

Indeed, the proposed hybrid scheme can autonomously switch between local and global power-sharing modes. Specifically, when all BSSs reach their nominal power, all compensation powers reach the limits and are identical. That is, the same compensation is added to each individual BSS, which is equivalent to the case without local compensation (i.e., global power-sharing mode). Mathematically, since the row sum of $\boldsymbol{L}_A$ is zeros (i.e., $\boldsymbol{L}_A\boldsymbol{1}_N=\boldsymbol{0}_N$), if $sat\left(p_i^c(t)\right)=1$ for $\forall i\in\mathcal{N}$, the convergence point is degraded from local power-sharing mode (8) to global power-sharing mode (6). Analogously, when any of the saturators leaves the boundary, the effect of local compensation gradually reappears, and the system switches back to the local power-sharing mode.

III. Stability Analysis and Optimal Design of Control Gains

In this section, the stability and optimality of the proposed hybrid scheme are analyzed. Stability analysis theoretically proves the system convergence, and optimality study deter-

mines the parameter settings of the proposed hybrid scheme to achieve the desired power-sharing distribution at the steady-state consensus and the dynamic performance along the trajectory to the steady-state consensus.

A. Stability Analysis

Previous studies in [39], [40] have theoretically proven that, with a connected neighboring communication network, global power-sharing droop-free controlled microgrids (5) are asymptotically stable, as stated in Lemma 0.

Lemma 0 [39], [40]: with a connected communication network, the global power-sharing droop-free controlled microgrid (5) is asymptotically stable. That is, for the system matrix $-h\boldsymbol{B}\boldsymbol{L}_A\boldsymbol{D}_p$ with $h>0$, it has a simple zero eigenvalue, and the real parts of all other $N-1$ effective eigenvalues are negative.

Based on this, stability proofs of the proposed local power-sharing droop-free control scheme and the hybrid local-global power-sharing scheme are further conducted. For the designed control systems (5) and (9), the state-space equation is derived as in (10), which is the focused system dynamics in the primary control layer. To effectively assess the impact of nonlinearity in (10) introduced by the saturator, the stability analysis is first conducted by exploring the system stability under three exclusive states: strict global power-sharing state, strict local power-sharing state, and autonomous mode-transition state.

$$\begin{bmatrix}\dot{\boldsymbol{p}}^n\\ \dot{\boldsymbol{p}}^c\end{bmatrix}=\begin{bmatrix}-h\boldsymbol{B}\boldsymbol{L}_A\left(\boldsymbol{D}_p\boldsymbol{p}^n-\boldsymbol{D}_p\boldsymbol{p}^d-sat\left(\boldsymbol{p}^c\right)\right)\\ k\left(\boldsymbol{D}_p\boldsymbol{p}^n-\boldsymbol{D}_p\boldsymbol{p}^d-sat\left(\boldsymbol{p}^c\right)\right)-e\cdot dzn\left(\boldsymbol{p}^c\right)\end{bmatrix} \tag{10}$$

Definition 1: ① strict global power-sharing state refers to that all the saturators reach the limits; ② strict local power-sharing state refers to that all the saturators are not activated; and ③ autonomous mode-transition state refers to that part of saturators reach the limits.

Lemma 1: if $e\gg k$, the proposed hybrid scheme is asymptotically stable in the strict global power-sharing state.

Proof: in the strict global power-sharing state, if $e\gg k$, $\boldsymbol{p}^c$ will be suppressed on the boundary since the anti-windup feedback dominates the integrator, and the system state-space equation (10) can be equivalently expressed as in (11). Because $\boldsymbol{L}_A\boldsymbol{1}_N=\boldsymbol{0}_N$, (11) can be further reduced to (12), which has the same system matrix $-h\boldsymbol{B}\boldsymbol{L}_A\boldsymbol{D}_p$ as the global power-sharing droop-free control (5). Thus, according to Lemma 0, the proposed hybrid scheme is asymptotically stable in the strict global power-sharing state.

$$\begin{bmatrix}\dot{\boldsymbol{p}}^n\\ \dot{\boldsymbol{p}}^c\end{bmatrix}=\begin{bmatrix}-h\boldsymbol{B}\boldsymbol{L}_A\left(\boldsymbol{D}_p\boldsymbol{p}^n-\boldsymbol{D}_p\boldsymbol{p}^d-\boldsymbol{1}_N\right)\\ \boldsymbol{0}_N\end{bmatrix} \tag{11}$$

$$\dot{\boldsymbol{p}}^n=-h\boldsymbol{B}\boldsymbol{L}_A\boldsymbol{D}_p\left(\boldsymbol{p}^n-\boldsymbol{p}^d\right) \tag{12}$$

Lemma 2: if $k>0$, the proposed hybrid scheme is asymptotically stable in the strict local power-sharing state.

Proof: as all saturators are not activated under the strict local power-sharing state, we have $sat\left(\boldsymbol{p}^c\right)=\boldsymbol{p}^c$ and $dzn\left(\boldsymbol{p}^c\right)=\boldsymbol{0}_N$ in (10). Thus, the system state-space equation (10) can be equivalently expressed as in (13).

$$\begin{bmatrix}\dot{\boldsymbol{p}}^n\\ \dot{\boldsymbol{p}}^c\end{bmatrix}=\begin{bmatrix}-h\boldsymbol{B}\boldsymbol{L}_A\left(\boldsymbol{D}_p\boldsymbol{p}^n-\boldsymbol{D}_p\boldsymbol{p}^d-\boldsymbol{p}^c\right)\\ k\left(\boldsymbol{D}_p\boldsymbol{p}^n-\boldsymbol{D}_p\boldsymbol{p}^d-\boldsymbol{p}^c\right)\end{bmatrix} \tag{13}$$

As both $\dot{\boldsymbol{p}}^c$ and $\dot{\boldsymbol{p}}^n$ depend on $\boldsymbol{D}_p\boldsymbol{p}^n-\boldsymbol{D}_p\boldsymbol{p}^d-\boldsymbol{p}^c$, the change of $\boldsymbol{p}^c$ and $\boldsymbol{p}^n$ are linearly dependent as in (14), where $\tilde{\boldsymbol{p}}^n=\boldsymbol{p}^n-\boldsymbol{p}^{n^*}$ denotes the change of dynamic variable $\boldsymbol{p}^n$ with respect to the steady-state $\boldsymbol{p}^{n^*}$. Because of the linear dependence, the system state-space equation (13) can be equivalently expressed as in (15) by substituting variables $\tilde{\boldsymbol{p}}^c$ with $\tilde{\boldsymbol{p}}^n$. $\tilde{\boldsymbol{p}}^d$ can be neglected since disturbances such as load changes as well as solar PV and wind power outputs are regarded as exogenous signals of the control system, i.e., $\boldsymbol{p}^d=\boldsymbol{p}^{d*}$ and $\tilde{\boldsymbol{p}}^d=\boldsymbol{0}_N$ after a disturbance.

$$\tilde{\boldsymbol{p}}^n=-\left(h/k\right)\boldsymbol{B}\boldsymbol{L}_A\tilde{\boldsymbol{p}}^c \tag{14}$$

$$\dot{\tilde{\boldsymbol{p}}}^n=-\left(h\boldsymbol{B}\boldsymbol{L}_A\boldsymbol{D}_p+k\boldsymbol{I}\right)\tilde{\boldsymbol{p}}^n \tag{15}$$

Denoting the eigenvalues of global power-sharing droop-free control (5) as λ_i^g, (15) indicates that eigenvalues of the strict local power-sharing state are equal to λ_i^g-k. As the real parts of λ_i^g are non-negative according to Lemma 0, the real parts of λ_i^g-k for $k>0$ are negative. Thus, the system is asymptotically stable in the strict local power-sharing state.

Lemma 3: the proposed hybrid scheme is asymptotically stable in the autonomous mode-transition state if $k>0$.

Proof: during the mode-transition state, BSSs can be divided into two exclusive sets $\mathcal{U}$ and $\mathcal{S}$. $|\mathcal{U}|$ denotes the number of BSSs in set $\mathcal{U}$. For the sake of discussion, we index the first $|\mathcal{U}|$ BSSs in set $\mathcal{N}$ belonging to $\mathcal{U}$ and the rest constituting $\mathcal{S}$. Besides, the state-space equations (12) and (15) imply that if the saturator at node i is activated, $K(i,i)$ is equal to 0; otherwise, $K(i,i)$ is equal to k. Consequently, the state-space equation of the mode-transition state can be expressed as in (16), where $\boldsymbol{I}_{|\mathcal{U}|}$ is an identity matrix of dimension $|\mathcal{U}|$.

$$\dot{\tilde{\boldsymbol{p}}}^n=-\left(h\boldsymbol{B}\boldsymbol{L}_A\boldsymbol{D}_p+k\begin{bmatrix}\boldsymbol{I}_{|\mathcal{U}|} & \boldsymbol{0}\\ \boldsymbol{0} & \boldsymbol{0}\end{bmatrix}\right)\tilde{\boldsymbol{p}}^n \tag{16}$$

The converse theorem [29] states that a formation of the Lyapunov energy function must exist for any asymptotically stable system. Taking the strict global power-sharing state (12) as an example, because it is asymptotically stable according to Lemma 1, a non-negative Lyapunov energy function L^g must exist as in (17a), and its trajectory $\dot{L}^g$ must be negative as in (17b).

$$L^g=\left(\tilde{\boldsymbol{p}}^n\right)^{\mathrm{T}}\boldsymbol{\mathcal{W}}\tilde{\boldsymbol{p}}^n\geq 0 \tag{17a}$$

$$\dot{L}^g=-2h\left(\tilde{\boldsymbol{p}}^n\right)^{\mathrm{T}}\boldsymbol{\mathcal{W}}\boldsymbol{B}\boldsymbol{L}_A\boldsymbol{D}_p\tilde{\boldsymbol{p}}^n<0 \tag{17b}$$

The Lyapunov energy function for autonomous mode-transition L^a can be similarly constructed to obtain the property of non-negativity, and its trajectory $\dot{L}^a$ can be derived as in (18). The trajectory includes two terms. The first term is the same as (17b), which is negative, and the positive definite matrix $\boldsymbol{\mathcal{W}}$ guarantees the non-positive of the second term with any positive k. Hence, $\dot{L}^a$ is always negative, and the system is asymptotically stable in the autonomous mode-transition state.

$$\dot{L}^a = -2h\left(\tilde{\boldsymbol{p}}^n\right)^{\mathrm{T}}\boldsymbol{\mathcal{W}}\boldsymbol{B}\boldsymbol{L}_A\boldsymbol{D}_p\tilde{\boldsymbol{p}}^n - 2k\left(\tilde{\boldsymbol{p}}^n\right)^{\mathrm{T}}\begin{bmatrix}\boldsymbol{I}_{|\mathcal{U}|} & \boldsymbol{0}\\ \boldsymbol{0} & \boldsymbol{0}\end{bmatrix}\boldsymbol{\mathcal{W}}\begin{bmatrix}\boldsymbol{I}_{|\mathcal{U}|} & \boldsymbol{0}\\ \boldsymbol{0} & \boldsymbol{0}\end{bmatrix}\tilde{\boldsymbol{p}}^n \tag{18}$$

Proposition 1: the designed system is stable if $0<h$ and $0<k\ll e$.

Proof: Lemmas 1-3 prove the asymptotic stability for all the three potential states when $0<h$ and $0<k\ll e$. Thus, it can be directly concluded that the proposed hybrid scheme is stable when $0<h$ and $0<k\ll e$.

B. Optimality of Local Power-sharing Distribution

Besides guaranteeing the system stability, the proposed hybrid scheme shall also pursue optimal performance goals. This subsection first studies the parameter settings for optimizing the local power-sharing distribution.

Equation (14) depicts the dependence between $\tilde{\boldsymbol{p}}^c$ and $\tilde{\boldsymbol{p}}^n$ during the dynamic process. It also indicates that the difference between the two steady states before and after disturbance shall satisfy (19):

$$\Delta\boldsymbol{p}^n = -r\boldsymbol{B}\boldsymbol{L}_A\Delta\boldsymbol{p}^c \tag{19}$$

where $\Delta\boldsymbol{p}^c=\boldsymbol{p}^{c*-}-\boldsymbol{p}^{c*}$ is the change of compensation power; $\Delta\boldsymbol{p}^n=\boldsymbol{p}^{n*-}-\boldsymbol{p}^{n*}$ is the change of nodal power; and $r=h/k$.

As for (13), the system reaches the equilibrium point at $\boldsymbol{D}_p\boldsymbol{p}^n-\boldsymbol{D}_p\boldsymbol{p}^d-\boldsymbol{p}^c=\boldsymbol{0}_N$. Thus, the steady states before and after disturbance shall satisfy (20a) and (20b), respectively. The difference between the two steady states shall further meet (20c).

$$\boldsymbol{D}_p\boldsymbol{p}^{n*-}-\boldsymbol{D}_p\boldsymbol{p}^{d*-}-\boldsymbol{p}^{c*-}=\boldsymbol{0}_N \tag{20a}$$

$$\boldsymbol{D}_p\boldsymbol{p}^{n*}-\boldsymbol{D}_p\boldsymbol{p}^{d*}-\boldsymbol{p}^{c*}=\boldsymbol{0}_N \tag{20b}$$

$$\boldsymbol{D}_p\Delta\boldsymbol{p}^n-\boldsymbol{D}_p\Delta\boldsymbol{p}^d-\Delta\boldsymbol{p}^c=\boldsymbol{0}_N \tag{20c}$$

where $\Delta\boldsymbol{p}^d=\boldsymbol{p}^{d*-}-\boldsymbol{p}^{d*}$ is the imposed exogenous disturbances such as the changes of loads as well as solar PV and wind power outputs.

Because $\boldsymbol{D}_p\boldsymbol{p}^n-\boldsymbol{D}_p\boldsymbol{p}^d=\boldsymbol{p}^{\bar{b}}$ holds in the dynamic system as shown in Fig. 2, (20b) and (20c) can be further rewritten as in (21a) and (21b), respectively.

$$\boldsymbol{p}^{\bar{b}*}=\boldsymbol{p}^{c*} \tag{21a}$$

$$\Delta\boldsymbol{p}^{\bar{b}}=\Delta\boldsymbol{p}^c \tag{21b}$$

Remark: according to (19) and (20c), when facing an exogenous disturbance $\Delta\boldsymbol{p}^d$, parameter r will solely determine the changes of compensation power and nodal power, forming the local power-sharing distribution. Thus, optimal power-sharing can be established by seeking the optimal r to properly distribute the disturbance to individual nodes.

Proposition 2: the optimal local power-sharing distribution against system-wide disturbances can be formulated as an optimization problem (22)-(23c), where the local power-sharing equalities in (23a) - (23c) are derived based on (19) - (21). Thus, minimizing the first term in (22) can pursue an even distribution of the power balance burden, minimizing the second term can chase the least power-shifting amount, and the weight ρ^I leverages the impacts of the power balance and power shifting burdens. Solving (22) - (23c) will derive the value of r that optimizes the power-sharing distribution.

$$\min\ \mathcal{J}^{\mathrm{I}}=\sum_{i\in\mathcal{N}}\left(\Delta\boldsymbol{p}^{\bar{b},i}\right)^{\mathrm{T}}\Delta\boldsymbol{p}^{\bar{b},i}+\rho^{\mathrm{I}}\left(\Delta\boldsymbol{p}^{n,i}\right)^{\mathrm{T}}\Delta\boldsymbol{p}^{n,i} \tag{22}$$

$$\Delta\boldsymbol{p}^{n,i}=-r\boldsymbol{B}\boldsymbol{L}_A\Delta\boldsymbol{p}^{c,i}\quad i\in\mathcal{N} \tag{23a}$$

$$\boldsymbol{D}_p\Delta\boldsymbol{p}^{n,i}-\boldsymbol{D}_p\Delta\boldsymbol{p}^{d,i}-\Delta\boldsymbol{p}^{c,i}=\boldsymbol{0}_N\quad i\in\mathcal{N} \tag{23b}$$

$$\Delta\boldsymbol{p}^{c,i}=\Delta\boldsymbol{p}^{\bar{b},i}\quad i\in\mathcal{N} \tag{23c}$$

C. Optimal Control for Dynamic Performance

This subsection further delves into the optimal control gains for ensuring the system's dynamic performance along the trajectory towards the consensus, guiding the system smoothly methods to the equilibrium with minimum power and frequency deviations.

The relative power positions between the neighboring BSSs $\tilde{\boldsymbol{p}}^p$ can be expressed as in (24a). According to the property of linear dependence (14) and $r=h/k$, (24a) can be equivalently converted to (24b).

$$\tilde{\boldsymbol{p}}^p=\boldsymbol{L}_A\left(\boldsymbol{D}_p\tilde{\boldsymbol{p}}^n-\tilde{\boldsymbol{p}}^c\right) \tag{24a}$$

$$\tilde{\boldsymbol{p}}^p=-\boldsymbol{L}_A\left(r\boldsymbol{D}\boldsymbol{B}\boldsymbol{L}_A+\boldsymbol{I}\right)\tilde{\boldsymbol{p}}^c \tag{24b}$$

Proposition 3: the optimal control for achieving the best dynamic performance can be modeled as in (25), where $\tilde{\boldsymbol{\omega}}=-h\tilde{\boldsymbol{p}}^{\bar{b}}$ is the nodal frequency deviation as described in (4). The first term in (25) calculates the gross power deviation during the convergence, and the second term quantifies the gross frequency deviation during the convergence. Weight ρ^{II} trades off the impacts of the two deviations. Furthermore, the optimal solution of (25) can be calculated as in (26).

$$\min\ \mathcal{J}^{\mathrm{II}}=\int_0^\infty\tilde{\boldsymbol{p}}^{p\,\mathrm{T}}\tilde{\boldsymbol{p}}^p+\rho^{\mathrm{II}}\tilde{\boldsymbol{\omega}}^{\mathrm{T}}\tilde{\boldsymbol{\omega}}\mathrm{d}t \tag{25}$$

$$k=\frac{1}{\sqrt{\rho^{\mathrm{II}}r}} \tag{26a}$$

$$h=\frac{1}{\sqrt{\rho^{\mathrm{II}}}} \tag{26b}$$

The proof of Proposition 3 is given in Appendix A.

D. Implementation

Based on the above discussions on the parameters and control gains to meet the requirements of system stability, power-sharing distribution, and dynamic trajectory, the guidance to the practical implementation of the proposed hybrid scheme can be conducted via the following steps.

Step 1: build the line susceptance matrix $\boldsymbol{B}$ and the adjacency matrix of neighboring communication $\boldsymbol{A}$ according to the microgrid topology.

Step 2: set the weights in the optimization. ρ^I can be selected in a wide range of [0.6, 1.4] based on extensive sensitivity analyses, where a large ρ^I limits the spread of disturbance and prefers the local power balance. ρ^{II} is recommended to be 10 to properly retain frequency fluctuations within ±50 mHz of the nominal value [13].

Step 3: solve parameter r via Proposition 2.

Step 4: solve control gains k and h via Proposition 3.

Step 5: set control gain e as $10k$, which is regarded as large enough to meet the requirement in Proposition 1.

IV. Case Studies

This section, by modifying the IEEE 34-node system [41], [42] to an islanded microgrid as shown in Fig. 3, illustrates the effectiveness of the proposed hybrid scheme in fulfilling the expected control performance and validates the conclusions derived from Propositions 1-3. The proposed hybrid scheme is further compared with the classical global power-sharing scheme [15] to present its merits in convergence speed and scalability. All the studies are implemented in Simulink. To focus on the discussed primary control layer, slower control layers such as secondary control [43] and tertiary control [44] are omitted in the simulation process, and faster control layers [45] such as inner voltage and current loops of VSIs are well-tuned.

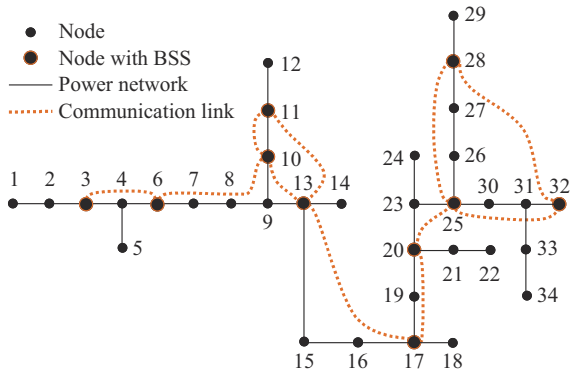

Fig. 3. Modified IEEE 34-node system.

For the modified IEEE 34-node system, the nominal nodal voltage is 4.16 kV. The nodes equipped with BSSs are coordinated via the neighboring communication links. The essential parameters of the system are given in Table I.

TABLE I
Essential Parameters of System

Parameter type	Parameter name	Value
System parameters	System nominal frequency	60 Hz
	System nominal voltage	4.16 kV
	Rated power of BSS	500 kW
	Nominal power of BSS	200 kW
	Filter time constant of control output	0.02 s
	Communication latency	Below 10 ms
	Communication frequency	Above 20 Hz
Optimization parameters	Power distribution weight ρ^{I}	0.65
	Dynamic performance weight ρ^{II}	10
Control parameters	Control gain ratio r	0.0325
	Compensation control gain k	9.7426
	Anti-windup control gain e	100
	Droop-free control gain h	0.3162

In Table I, the control gains are calculated according to Propositions 1-3. Additionally, to clearly show the effects of the proposed hybrid scheme for active power-sharing, the classic droop-free control [15] is adopted for reactive power-sharing in the simulation.

A. Global and Local Power-sharing Modes and Their Transitions

For the sake of illustration, we assume that at the initial status of the simulation, the supply and demand of the microgrid are balanced, and the power outputs of BSSs are all 0. A series of disturbances occurring at different nodes are simulated via a combination of constant impedence, constant current, and constant power elements [46], in which the changes of solar PV and wind power outputs are simulated through net load changes of constant power components. Specifically, starting from 10 s, a sequence of 400 kW net load increase occurs at node 18 every 20 s; then the net load turns to decline at 150 s and 170 s. The response of the BSSs against net load disturbances at node 18 is shown in Fig. 4. It can be observed that the system can properly share the power burden in both local and global power-sharing modes and autonomously transit between the two modes at the appropriate system operation state.

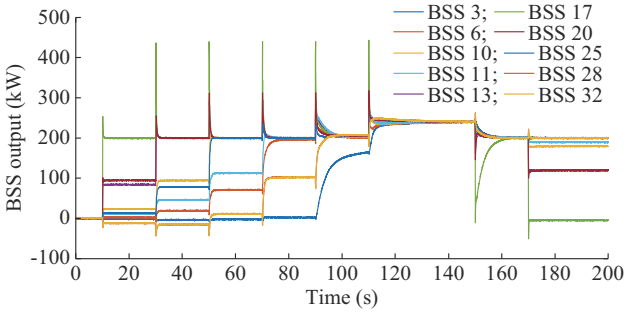

Fig. 4. Response of BSSs against net load disturbances at node 18.

When the net load increases at 10 s, the closest BSS 17 instantaneously undertakes most disturbance and promptly shares with the other BSSs until balancing roughly 50% of the disturbance, while BSSs 13 and 20 that directly communicate with BSS 17 share 20.9% and 23.5% of the disturbance, respectively. The slight difference in power-sharing of BSSs 13 and 20 is affected by the network topology and impedance of power lines, as reflected by the optimized control gains. Besides, all other BSSs indirectly communicating with BSS 17 collectively take the remaining 5.6% disturbance. It clearly shows that the power distribution meets the expected control performance of local power-sharing.

With the continuous net load increase, the control system spreads power-sharing to farther BSSs. At 100 s, all BSSs except the farthest BSS 3 have arrived at their nominal power levels, and the system remains operated in local power-sharing mode. When another 400 kW disturbance occurs at node 18, all BSSs reach their nominal power levels and the system switches to the global power-sharing mode. It clearly shows that: ① the system is smoothly switched from the local to global power-sharing mode between 100-120 s without abnormal perturbation; and ② the mode change is autonomously activated according to the system operation condition.

When the net load decreases at 150 s, the system remains operation in global power-sharing mode, and all BSSs reduce their power outputs evenly. Another net load decline at

170 s drives the system to autonomously switch back to the local power-sharing mode, where BSS 17 preferentially takes about half of the net load decrease onsite, meeting the local power-sharing requirement that closer BSS shares more disturbances.

The detailed control signals during the dynamic process including saturated compensation power, compensation power, communicated request, and nodal frequencies are plotted in Fig. 5. The power-related signals are presented in per-unit values which are converted through the normalization process using the nominal power as the base.

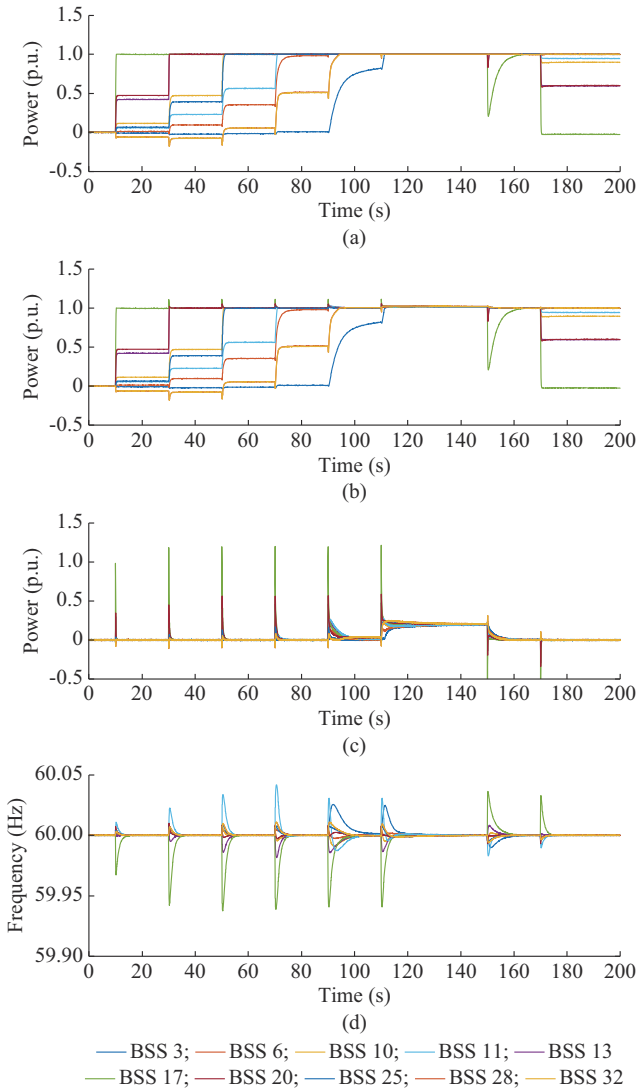

Fig. 5. Detailed control signals during dynamic process. (a) Saturated compensation power $sat\left(\boldsymbol{p}^{c}\right)$. (b) Compensation power $\boldsymbol{p}^{c}$. (c) Communicated request $\boldsymbol{p}^{\bar{b}}-sat\left(\boldsymbol{p}^{c}\right)$. (d) Nodal frequencies.

Figure 5(a) shows that the compensation power can always be timely and smoothly trimmed below the nominal power through the saturator. If any of the compensations is not saturated, the microgrid operates in the local power-sharing mode, and the maximum shared power is limited below the nominal power in 0-100 s, as shown in Fig. 4. If all compensation power reaches the limits, the identical compensation is added to individual BSSs, and the microgrid transits to the global power-sharing mode in 120-150 s, as shown in Fig. 4.

The untrimmed compensation power signal is further extracted in Fig. 5(b). Compared with Fig. 5(a), it shows that the anti-windup controller is able to rapidly suppress the buffer in calculating the compensation power and harmonize the values of trimmed and untrimmed compensation power. Otherwise, the buffer will lead the recovery response to be inactive when encountering the negative disturbance.

The communicated request $\boldsymbol{p}^{\bar{b}}-sat\left(\boldsymbol{p}^{c}\right)$ is shown in Fig. 5(c). In the local power-sharing mode, all requests converge to 0, indicating that $\boldsymbol{p}^{\bar{b}*}=sat\left(\boldsymbol{p}^{c*}\right)=\boldsymbol{p}^{c*}$ as shown in (21), which means the power-sharing strictly follows the guidance of local compensation power. In comparison, the elements in vector $\boldsymbol{p}^{\bar{b}}-sat\left(\boldsymbol{p}^{c}\right)$ move towards 0.2 p.u. during 120-150 s, where $sat\left(\boldsymbol{p}^{c}\right)$ reaches 1 according to Fig. 5(a). Hereby, all normalized BSS outputs $\boldsymbol{p}^{\bar{b}}$ converge to 1.2 p.u. during that period, showing that power-sharing strictly follows the guidance of global compensation power. Thus, both local and global modes can precisely achieve the consensus in the proposed hybrid scheme.

In addition, the nodal frequency dynamics are shown in Fig. 5(d). In response to the series of sharp net load changes, the frequency can be smoothly regulated. During the process, the frequencies of several inverter-interfaced BSSs are adjusted above 60 Hz, while the others are reduced below 60 Hz. Based on further numerical calculations, the system frequency can be maintained at 60 Hz. Thus, the results demonstrate that the proposed hybrid scheme can achieve the droop-free control target.

To clearly show the effects of the proposed hybrid scheme for active power-sharing, the classic droop-free control model [15] is adopted for reactive power-sharing in this simulation, i. e., reactive power fluctuations are proportionally shared according to the capacities of controllable resources to globally average the reactive power burden. The simulation results are recorded in Fig. 6, in which each 400 kW active power disturbance at node 18 carries 80 kvar reactive power change.

As shown in Fig. 6(a), the reactive power fluctuation can be accurately shared among all controllable resources that each BSS proportionally undertakes 8.0 kvar reactive power change. During the dynamics shown in Fig. 6(b), several nodal voltages are regulated below 4.16 kV, while the others are raised to ensure the average value of all nodal voltages is kept at the nominal value of 4.16 kV, realizing the reactive power-sharing in a voltage droop-free control process.

B. System Performance Against Random Disturbances

Power-sharing mainly copes with disturbances in the primary control. In the simulation, 1000 random disturbances with magnitudes between −40 kW and 40 kW occurring at arbitrary nodes are generated, as shown in Fig. 7.

In Fig. 7, the maximum accumulated magnitude of nodal disturbances is around 420 kW, and the total disturbance mileage [47] amounts to 20 MW for the entire simulation time window. The response of BSSs in the proposed hybrid scheme is shown in Fig. 8.

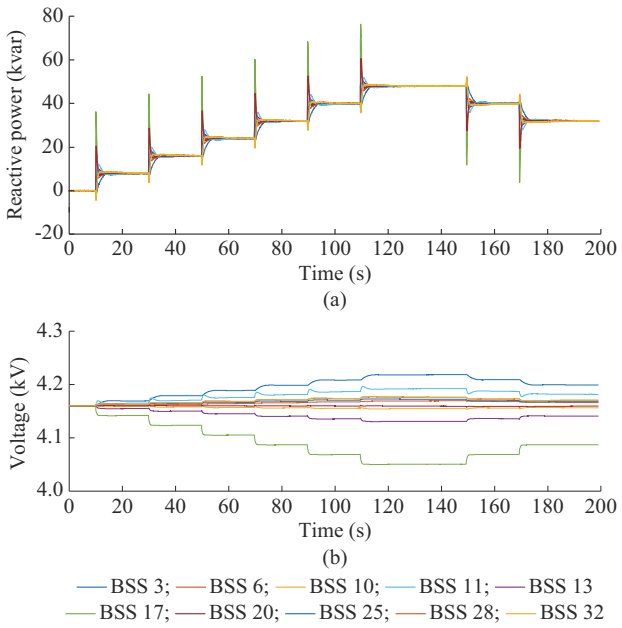

Fig. 6. Responses of reactive power distribution and nodal voltages. (a) Reactive power distribution. (b) Nodal voltages.

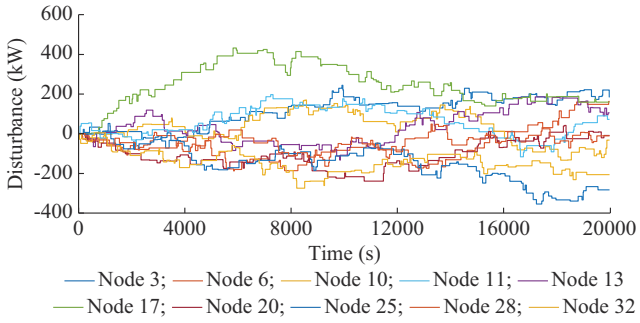

Fig. 7. Generated random disturbances at individual nodes.

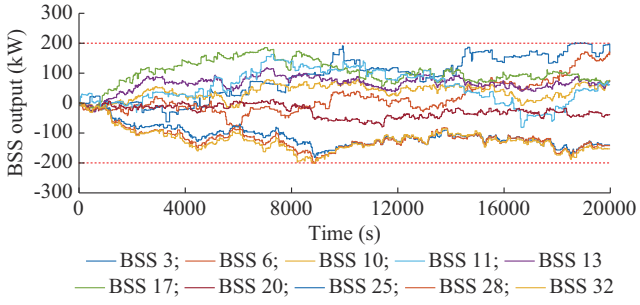

Fig. 8. Response of BSSs in proposed hybrid scheme.

Indeed, distributed controlled BSSs can collaboratively seek the optimal sharing results against multiple disturbances at different locations via the sparse neighboring communication network, and the system is capable of properly operating within the nominal power levels and compensating individual disturbances in a local power-sharing way.

To further analyze the distribution of local power-sharing, Fig. 9 plots the relationship between the proportion of disturbances shared by individual BSSs versus the maximum propagation steps, where the maximum propagation steps refer to the largest number of neighboring communication propagations needed from between two BSSs. In Fig. 9, the top blue line presents that BSS 3 retains 85.4% disturbance onsite, while sharing the rest 24.6% with all other BSSs. Since BSS 3 is the most remote BSS in the microgrid with only one neighbor (i. e., BSS 6) connected through a long electrical line (i. e., 13.2 miles between nodes 3 and 6), the response curve of BSS 3 is the topmost. In comparison, BSS 25 with three close neighbors (the electrical lines from BSS 25 to BSSs 20, 28, and 32, are 2.0, 1.0, and 1.05 miles, respectively) can allocate disturbance more evenly in a proper local region, i. e., 27.8% for itself and 23.2% in average for the three neighbors. These results show that the local power-sharing control can properly utilize the neighboring resources and effectively retain the impact of disturbance within a small region.

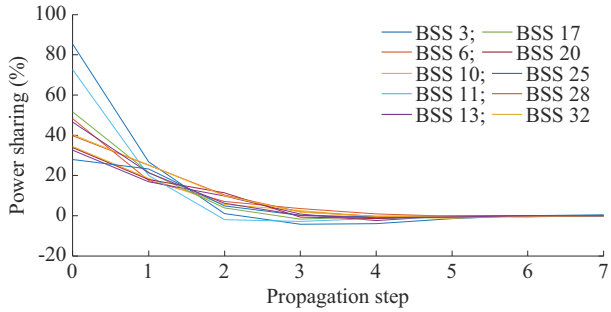

Fig. 9. Distribution of power-sharing for individual BSSs.

The optimal power-sharing distribution is reached with the control gain ratio $r=0.0325$ according to Proposition 2. On this basis, additional simulations are conducted by tuning r around the optimal value. Responding to the disturbances in Fig. 7, the simulated total power-sharing burdens $\mathcal{J}^1$ are recorded in Table II, including the power balance burden and the power shifting burden as defined in (22). All results are in per-unit values using the optimal value with $r^*=0.0325$ as the base for clear comparison. It is noteworthy that $r=\infty$ (i.e., $k\approx 0$) is the global power-sharing case, because the compensation controllers are not activated.

TABLE II
POWER-SHARING BURDENS

Parameter	Balance burden (p.u.)	Shifting burden (p.u.)	Total burden (p.u.)
$0.125r^*$	0.943	0.147	1.090
$0.25r^*$	0.790	0.238	1.028
$0.5r^*$	0.660	0.342	1.002
$0.75r^*$	0.596	0.403	0.999
r^*	0.555	0.445	1.000
$2r^*$	0.472	0.537	1.009
$4r^*$	0.406	0.614	1.020
$8r^*$	0.352	0.676	1.027
∞	0.157	0.919	1.076

Table II shows that as r increases, more disturbances are undertaken by remote BSSs and the system moves towards global power-sharing, presenting a lower balance burden and

higher shifting burden.

Overall, although setting the parameter as $0.75r^*$ is a better choice in this simulated system, the solution solved by Proposition 2 with merely a 0.13% higher objective value is admissible. It validates that the value r solved via Proposition 2 performs properly in trading off the impacts of power balance and power shifting burdens.

Moreover, according to Proposition 3, $h=0.316$ can provide the optimal trajectory moving towards the convergence point. In the simulation, different values of h are tested as shown in Table III. According to the tendency shown in Table III, a lower value of h presents a smaller control adjustment on nodal frequencies, which slows down the convergence process and accumulates the larger power deviation. On the other hand, increasing the droop-free control gain h can amplify the frequency adjustment, and in return accelerate the system convergence and decrease the accumulated power deviation therein. Simulation results verify that $h=0.316$ is the finest parameter considering both frequency and power deviations during the convergence process.

TABLE III
DEVIATION DURING CONVERGING DYNAMICS

Parameter	Frequency deviation (p.u.)	Power deviation (p.u.)	Total deviation (p.u.)
$0.25h^*$	0.103	1.655	1.759
$0.5h^*$	0.221	0.882	1.103
h^*	0.500	0.500	1.000
$2h^*$	1.246	0.312	1.558
$4h^*$	3.374	0.211	3.585

Finally, a stress test is further conducted to present the advantages of the proposed hybrid scheme over the local scheme. In the test, the total disturbance mileage is set to be 200 MW, 10 times the disturbances in Fig. 7. The responses of BSSs against 200 MW mileage disturbances in the local and hybrid schemes are plotted in Fig. 10(a) and 10(b), respectively.

Although the local scheme stably operates the system against disturbances, BSSs frequently operate above the rated power (i.e., the two red dotted lines describe the rated charging and discharging power levels) as shown in Fig. 10(a). At this zone, the energy loss grows exponentially along with the increase in the output level, leading to high operation costs. Besides, BSSs reach the rated power (500 kW) multiple times, making the system vulnerable to new disturbances.

In comparison, in the hybrid scheme, BSSs can properly operate within the range of nominal power, achieving better operation efficiency. Although certain overshoots are unavoidable in dealing with large disturbances, the system can timely coordinate BSSs and quickly return to the effective zone. Besides, during certain periods with heavy disturbances, the system reasonably operates in the global power-sharing mode to even the burdens of BSSs. For example, the zoom-in sub-figure during the period of 7150-7350 s shows that the system smoothly switches to the global power-sharing mode to even the burdens of BSSs. After the disturbances decrease, the system automatically switches back to the local power-sharing mode, presenting the transition stability properties proved in Proposition 1.

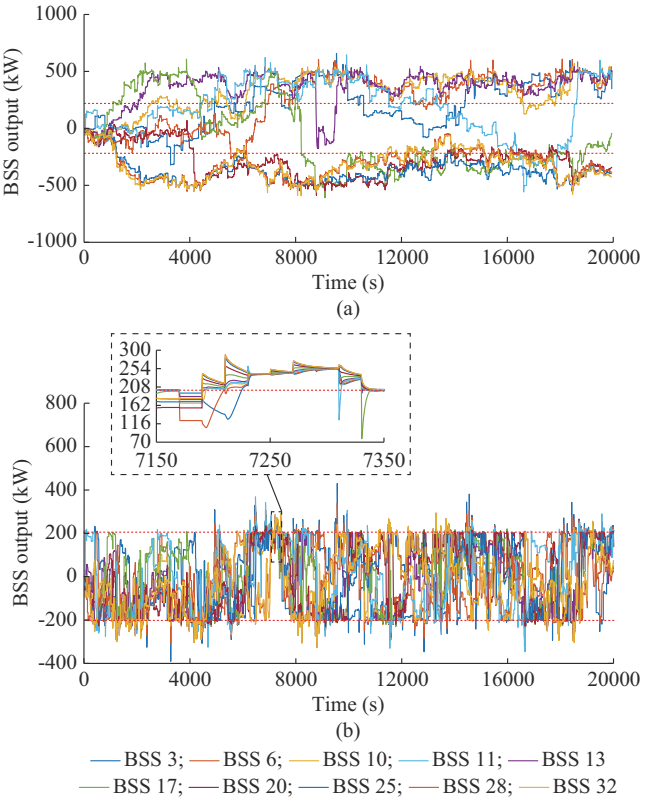

Fig.10. Responses of BSSs against 200 MW mileage disturbances. (a) Local scheme. (b) Hybrid scheme.

In summary, the simulation results validate the conclusions derived from Propositions 1-3 regarding the system stability as well as the optimality of power-sharing distribution at the steady-state consensus and dynamic performance along the trajectory to the steady-state consensus.

C. Scalability Improvement over Classical Global Power-sharing Scheme

In addition to properly distributing disturbances locally, another essential merit of the local power-sharing mode is to accelerate the convergence speed of the neighboring communication-based droop-free control. The classical global power-sharing scheme to reach the system-wide consensus is time-consuming. In comparison, the local power-sharing by retaining the response in a small region and reducing the number of involved BSSs in the coordination process can accelerate the convergence speed.

The original system in Fig. 3 is scaled up to Fig. 11 with extra BSSs to illustrate the convergence speed of the proposed local power-sharing scheme. BSSs at the orange nodes connected through orange dashed lines form the benchmark system. The maximum steps of propagation in the benchmark system are 5, e.g., a disturbance occurring at node 32 is first balanced by BSS 32, and gradually propagated to BSS 10 through 5 neighboring communication steps. On this basis, the augmented cases, by adding BSSs 6, 3, 2, 1, and

the associated communication links, scale up the maximum steps of propagation from 5 to 6-9.

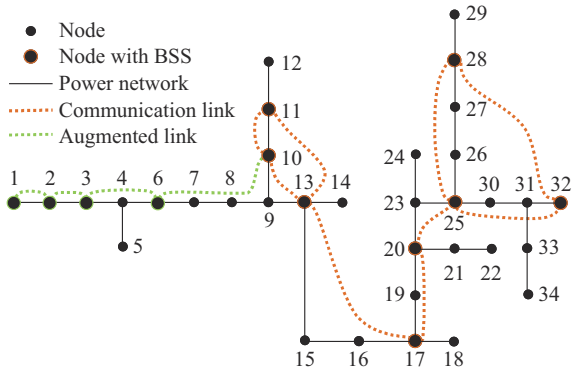

Fig. 11. Scaled BSSs in modified IEEE 34-node system.

The scaled system with the global and local power-sharing schemes is simulated against a 200 kW disturbance at arbitrary locations. When nodal states fall within the ±2 kW error band of the power-sharing consensus, the system is regarded as settled, and the average settling time is compared in Table IV.

TABLE IV
COMPARISON OF AVERAGE SETTLING TIMES

The maximum steps of propagation	Number of BSSs	Average settling time (s)		Global-to-local ratio
		Global sharing	Local sharing	
5	8	27.83	0.16	173.9
6	9	30.73	0.16	192.1
7	10	35.93	0.17	211.4
8	11	46.40	0.16	290.0
9	12	56.69	0.15	377.9

According to the results of the global power-sharing scheme, the settling time steadily increases as the system scales up, since more intermediate propagations are needed to evenly allocate disturbances among all BSSs. In contrast, the settling time of local power-sharing design is retained in the range of 0.15-0.17 s, and the system scale presents negligible impacts on the convergence speed.

Table IV clearly shows that the convergence speed of the local power-sharing scheme is about 173.9 to 377.9 times faster than the global power-sharing scheme. To further delve into this phenomenon, global and local power-sharing responses against a disturbance on node 32 are plotted in Figs. 12 and 13, respectively.

Figure 12 shows that the outputs of all BSSs have the same value while following different trajectories. Specifically, BSS 32 undertakes the largest proportion of disturbance initially, while the outputs of its two nearby BSSs 25 and 28 rapidly approach that of BSS 32. On the contrary, the outputs of BSSs 3, 6, 10, 11, and 13 increase rather slowly since they are relatively remote to BSS 32. After around 35.93 s, the system reaches a global power-sharing consensus, which is time-consuming by coordinating through the sparse neighboring communication network.

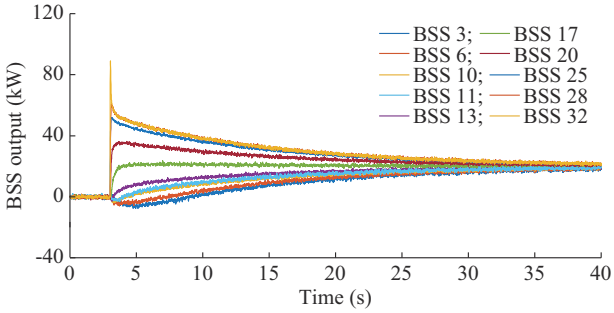

Fig. 12. Global power-sharing scheme.

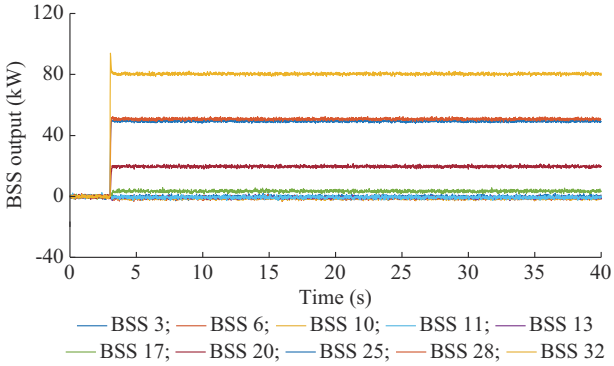

Fig. 13. Local power-sharing scheme.

In comparison, Fig. 13 shows that although the local power-sharing scheme presents a similar initial response as the global power-sharing scheme right after the disturbance occurs, it seizes the equilibrium power-sharing status in merely 0.17 s. Thus, the local power-sharing scheme is quantified as more efficient than continuously shifting power to other BSSs according to Proposition 2.

Moreover, the responses of nodal frequencies in different schemes during the dynamic process are recorded in Fig. 14.

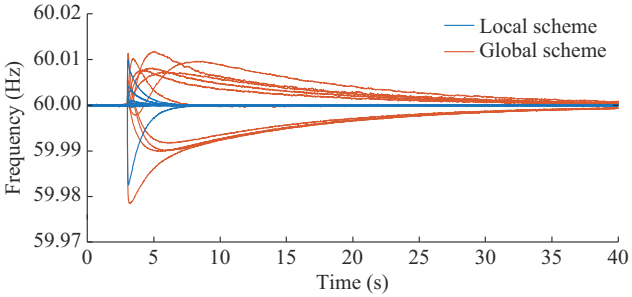

Fig. 14. Responses of nodal frequencies in different schemes.

When a disturbance occurs and is being shared within the network, the onsite BSS 32 in the two schemes presents the same largest rate of change of frequency (RoCoF) [48], since the identical set of droop-free control gains and disturbances are applied in both cases. The frequency nadir of the local power-sharing scheme is 59.983 Hz, which is 3.6 mHz higher than the global power-sharing scheme. In addition, local power-sharing scheme presents significant advantages in frequency settling time. These measurements clearly show that the local power-sharing scheme presents slightly better stability performance in frequency when BSSs operate with-

in the nominal power levels.

To sum up, the proposed hybrid scheme achieves fast convergence speed, less sensitivity to system sizes, increased cost-efficiency, and similar frequency stability, leading to enhanced droop-free control with superior scalability.

D. Convergence Performance over Communication Delays

The performance of neighboring communication based droop-free control is usually sensitive to communication delay. In the simulation, delay blocks are added between the communication processes of droop-free controllers. On this basis, communication delays ranging from 0.1 ms to 10000 ms are tested for comparison, as listed in Table V.

TABLE V
COMPARISON OF SETTLING TIME WITH DIFFERENT COMMUNICATION DELAYS

Communication delay (ms)	Settling time (s)	Communication delay (ms)	Settling time (s)
Instantaneous	0.215	50.0	0.460
0.1	0.215	100.0	1.220
0.5	0.215	500.0	9.530
1.0	0.215	1000.0	27.190
5.0	0.215	5000.0	235.370
10.0	0.215	10000.0	510.060

According to Table V, several observations can be obtained: ① the settling time can be retained at 0.215 s for the systems with a communication delay of less than 10 ms, where the systems can reach similar performance as the case without communication delay; ② as the communication delay increases, the settling time will be elongated. From 50 ms to 10000 ms, scaling up the delay by 10 times will increase the settling time by more than 20 times; and ③ the system can still converge even with a communication delay as large as 10000 ms (i.e., 10 s).

In addition, the response of nodal frequencies with typical communication delays of 10 ms, 100 ms, and 1000 ms is plotted in Fig. 15.

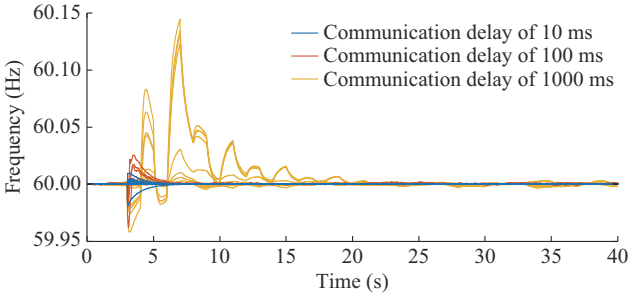

Fig. 15. Response of nodal frequencies with typical communication delays.

As the delay increases, the dynamic performance is significantly compromised in several aspects. Numerically, the frequency nadir is compromised to 59.983 Hz, 59.962 Hz, and 59.958 Hz, respectively; the highest frequency reaches 60.009 Hz, 60.025 Hz, and 60.145 Hz, respectively; and the largest RoCoF is recorded as 0.180 Hz/s, 0.359 Hz/s, and 0.3776 Hz/s, respectively. Besides, the yellow curves present significant oscillation at around 1000 ms, matching the communication delay level. It shows the dynamic performance of droop-free control will degenerate with high communication latency. Based on the above observations, system performance could be guaranteed with a communication delay of less than 10 ms. Besides, the system stability is robust against moderate communication delay (i. e., 10 s), at the cost of longer settling time.

V. CONCLUSION

Focusing on droop-free controlled microgrids, different from the global power-sharing design which distributes disturbance among all BSSs to average the nodal burden, this paper proposes a local power-sharing droop-free control scheme to properly retain disturbances in a small region. On this basis, a hybrid local-global power-sharing scheme is put forward to preserve the merits of both designs. Moreover, systematic guidance for control gain setup is derived based on stability analysis and optimal control to guide practical implementation.

Based on the theoretical analysis and numerical simulations, microgrids with the proposed hybrid scheme perform stably against disturbances, while following the least-deviation trajectory toward the desired power-sharing consensus. Moreover, the proposed hybrid scheme outperforms the classical global power-sharing in convergence speed and scalability, with steady settling times for microgrids of varied sizes.

Future works will implement the proposed hybrid scheme onto the hardware-in-the-loop (HIL) testbed to further verify and promote the practical application in renewable-centric microgrids.

APPENDIX A

Problem (25) can be equivalently converted to (A1) based on (24b) and $\tilde{\boldsymbol{\omega}}=-h\tilde{\boldsymbol{p}}^{p}$.

$$\min \mathcal{J}^{\mathrm{II}}=\int_{t_0}^{\infty}\left(1+\rho^{\mathrm{II}}r^2k^2\right)\left(\tilde{\boldsymbol{p}}^{c}\right)^{\mathrm{T}}\left(r\boldsymbol{D}\boldsymbol{B}\boldsymbol{L}_{A}+\boldsymbol{I}\right)^{\mathrm{T}}\cdot \boldsymbol{L}_{A}\boldsymbol{L}_{A}\left(r\boldsymbol{D}\boldsymbol{B}\boldsymbol{L}_{A}+\boldsymbol{I}\right)\tilde{\boldsymbol{p}}^{c}\mathrm{d}t \tag{A1}$$

We further reorganize (A1) and (15b) to (A2), (A3), where matrices $\boldsymbol{\mathcal{A}}$, $\boldsymbol{\mathcal{B}}$, $\boldsymbol{\mathcal{Q}}$, and $\boldsymbol{\mathcal{R}}$ can be derived as shown in (A4)-(A7).

$$\min \mathcal{J}^{\mathrm{II}}=\int_{t_0}^{\infty}\left(\tilde{\boldsymbol{p}}^{c}\right)^{\mathrm{T}}\left(\boldsymbol{\mathcal{Q}}+k^2\boldsymbol{\mathcal{R}}\right)\tilde{\boldsymbol{p}}^{c}\mathrm{d}t \tag{A2}$$

$$\dot{\tilde{\boldsymbol{p}}}^{c}=\boldsymbol{\mathcal{A}}\tilde{\boldsymbol{p}}^{c}-k\boldsymbol{\mathcal{B}}\tilde{\boldsymbol{p}}^{c} \tag{A3}$$

$$\boldsymbol{\mathcal{A}}=\boldsymbol{0} \tag{A4}$$

$$\boldsymbol{\mathcal{B}}=r\boldsymbol{D}_{p}\boldsymbol{B}\boldsymbol{L}_{A}+\boldsymbol{I} \tag{A5}$$

$$\boldsymbol{\mathcal{Q}}=\boldsymbol{\mathcal{B}}^{\mathrm{T}}\boldsymbol{L}_{A}\boldsymbol{L}_{A}\boldsymbol{\mathcal{B}} \tag{A6}$$

$$\boldsymbol{\mathcal{R}}=\rho^{\mathrm{II}}r^2\boldsymbol{\mathcal{Q}} \tag{A7}$$

With the objective function (A2) and the state-space equation (A3), a cost-to-go function $V_{\tilde{\boldsymbol{p}}^{c},t}$ can be established as shown in (A8), which describes the optimal trajectory from time t to the steady state. k is the control variable for the tra-

jectory.

$$V_{\tilde{\boldsymbol{p}}^c,t}=\min_k\left(\int_t^{\infty}\left(\tilde{\boldsymbol{p}}^c(\tau)\right)^{\mathrm{T}}\left(\boldsymbol{\mathcal{Q}}+k^2\boldsymbol{\mathcal{R}}\right)\tilde{\boldsymbol{p}}^c(\tau)\,\mathrm{d}\tau\right) \tag{A8}$$

Two decomposition methods are applied to (A8). First, $V_{\tilde{\boldsymbol{p}}^c,t}$ equals to the optimal trajectory from time t to $t+\mathrm{d}t$ plus the optimal trajectory from time $t+\mathrm{d}t$ to the steady state, as shown in (A9). Equation (A9) can be further simplified to (A10) with a small enough dt. Second, Taylor expansion is applied on (A8) to derive (A11).

$$V_{\tilde{\boldsymbol{p}}^c,t}=\min_k\left(\int_t^{t+\mathrm{d}t}\left(\tilde{\boldsymbol{p}}^c(\tau)\right)^{\mathrm{T}}\left(\boldsymbol{\mathcal{Q}}+k^2\boldsymbol{\mathcal{R}}\right)\tilde{\boldsymbol{p}}^c(\tau)\,\mathrm{d}\tau+V_{\tilde{\boldsymbol{p}}^c,t+\mathrm{d}t}\right) \tag{A9}$$

$$V_{\tilde{\boldsymbol{p}}^c,t}\approx\min_k\left(\left(\tilde{\boldsymbol{p}}^c\right)^{\mathrm{T}}\left(\boldsymbol{\mathcal{Q}}+k^2\boldsymbol{\mathcal{R}}\right)\tilde{\boldsymbol{p}}^c\,\mathrm{d}t+V_{\tilde{\boldsymbol{p}}^c,t+\mathrm{d}t}\right) \tag{A10}$$

$$V_{\tilde{\boldsymbol{p}}^c,t+\mathrm{d}t}\approx V_{\tilde{\boldsymbol{p}}^c,t}+\dot{V}_{\tilde{\boldsymbol{p}}^c,t}\mathrm{d}t \tag{A11}$$

Using (A11) to substitute $V_{\tilde{\boldsymbol{p}}^c,t+\mathrm{d}t}$ in (31) and further canceling dt derive the modified Hamilton-Jacobi-Bellman (HJB) equation (A12). Assuming a time-invariant matrix $\boldsymbol{\mathcal{P}}$ exists that $V_{\tilde{\boldsymbol{p}}^c,t}=\left(\tilde{\boldsymbol{p}}^c\right)^{\mathrm{T}}\boldsymbol{\mathcal{P}}\tilde{\boldsymbol{p}}^c$, (A12) can be converted to (A13).

$$0\approx\min_k\left(\dot{V}_{\tilde{\boldsymbol{p}}^c,t}+\left(\tilde{\boldsymbol{p}}^c\right)^{\mathrm{T}}\left(\boldsymbol{\mathcal{Q}}+k^2\boldsymbol{\mathcal{R}}\right)\tilde{\boldsymbol{p}}^c\right) \tag{A12}$$

$$0\approx\min_k\left(-2k\left(\tilde{\boldsymbol{p}}^c\right)^{\mathrm{T}}\boldsymbol{\mathcal{P}}\boldsymbol{\mathcal{B}}\tilde{\boldsymbol{p}}^c+\left(\tilde{\boldsymbol{p}}^c\right)^{\mathrm{T}}\left(\boldsymbol{\mathcal{Q}}+k^2\boldsymbol{\mathcal{R}}\right)\tilde{\boldsymbol{p}}^c\right) \tag{A13}$$

If matrix $\boldsymbol{\mathcal{P}}$ exists, the optimal solution of k could render the minimum value for $M=-2k\left(\tilde{\boldsymbol{p}}^c\right)^{\mathrm{T}}\boldsymbol{\mathcal{P}}\boldsymbol{\mathcal{B}}\tilde{\boldsymbol{p}}^c+\left(\tilde{\boldsymbol{p}}^c\right)^{\mathrm{T}}\left(\boldsymbol{\mathcal{Q}}+k^2\boldsymbol{\mathcal{R}}\right)\tilde{\boldsymbol{p}}^c$ in (A13). To address the minimum value, k is first solved via the extreme value theorem. That is, the first-order derivative of M must equal to 0 as shown in (A14), and the second-order derivative of M is non-negative as shown in (A15). Consequently, k is deduced as in (A16), depicting the relationship between $\boldsymbol{\mathcal{P}}$ and k.

$$\frac{\partial M}{\partial k}=-2\left(\tilde{\boldsymbol{p}}^c\right)^{\mathrm{T}}\left(\boldsymbol{\mathcal{P}}\boldsymbol{\mathcal{B}}-k\boldsymbol{\mathcal{R}}\right)\tilde{\boldsymbol{p}}^c=0 \tag{A14}$$

$$\frac{\partial^2 M}{\partial k^2}=2\left(\tilde{\boldsymbol{p}}^c\right)^{\mathrm{T}}\boldsymbol{\mathcal{R}}\tilde{\boldsymbol{p}}^c\geq 0 \tag{A15}$$

$$\boldsymbol{\mathcal{P}}\boldsymbol{\mathcal{B}}=k\boldsymbol{\mathcal{R}} \tag{A16}$$

Finally, to further verify whether the optimal solution of k can drive M to the minimum value 0, we substitute $\boldsymbol{\mathcal{P}}$ in (A15) via (A16) to derive (A17). Obviously, $\boldsymbol{\mathcal{Q}}=k^2\boldsymbol{\mathcal{R}}$ can meet (A17) for any $\tilde{\boldsymbol{p}}^c$. Since $\mathcal{R}=\rho^{\mathrm{II}}r^2\boldsymbol{\mathcal{Q}}$ as defined in (A7), the optimal solution k can be solved as $1\Big/\left(\sqrt{\rho^{\mathrm{II}}}\,r\right)$. The negative solution $-1\Big/\left(\sqrt{\rho^{\mathrm{II}}}\,r\right)$ is discarded because it is out of the stability range as proved in Proposition 1. Furthermore, the optimal solution $h=1\Big/\left(\sqrt{\rho^{\mathrm{II}}}\right)$ can be acquired as $r=h/k$.

$$0\approx\left(\tilde{\boldsymbol{p}}^c\right)^{\mathrm{T}}\left(\boldsymbol{\mathcal{Q}}-k^2\boldsymbol{\mathcal{R}}\right)\tilde{\boldsymbol{p}}^c \tag{A17}$$

REFERENCES

[1] U. S. Congress. (2021, Jun.). American Renewable Energy Act of 2021. [Online]. Available: https://www. congress. gov/bill/117th-congress/house-bill/3959/text?r=91&s=1

[2] European Commission. (2021, Jul.). Revision of Renewable Energy Directive. [Online]. Available: https://eur-lex. europa. eu/legal-content/EN/TXT/?uri=CELEX%3A52021PC0557

[3] K. Zuo and W. Lei, "A review of decentralized and distributed control approaches for islanded microgrids: novel designs, current trends, and emerging challenges," *The Electricity Journal*, no. 35, vol. 5, pp. 1-6, Jun. 2022.

[4] Q. Zhong and G. Weiss, "Synchronverters: inverters that mimic synchronous generators," *IEEE Transactions on Industrial Electronics*, vol. 58, no. 4, pp. 1259-1267, Apr. 2010.

[5] N. Harag, M. Imanaka, M. Kurimoto *et al.*, "Autonomous dual active power-frequency control in power system with small-scale photovoltaic power generation," *Journal of Modern Power Systems and Clean Energy*, vol. 10, no. 4, pp. 941-953, Jul. 2022.

[6] Y. Wang, F. Qiu, G. Liu *et al.*, "Adaptive reference power based voltage droop control for VSC-MTDC systems," *Journal of Modern Power Systems and Clean Energy*, vol. 11, no. 1, pp. 381-388, Jan. 2023.

[7] U. B. Tayab, M. A. B. Roslan, L. J. Hwai *et al.*, "A review of droop control techniques for microgrid," *Renewable and Sustainable Energy Reviews*, vol. 76, pp. 717-727, Sept. 2017.

[8] R. Razi, H. Iman-Eini, M. Hamzeh *et al.*, "A novel extended impedance-power droop for accurate active and reactive power sharing in a multi-bus microgrid with complex impedances," *IEEE Transactions on Smart Grid*, vol. 11, no. 5, pp. 3795-3804, Sept. 2020.

[9] W. Deng, N. Dai, K. Lao *et al.*, "A virtual-impedance droop control for accurate active power control and reactive power sharing using capacitive-coupling inverters," *IEEE Transactions on Industry Applications*, vol. 56, no. 6, pp. 6722-6733, Nov. 2020.

[10] P. Sreekumar and V. Khadkikar, "A new virtual harmonic impedance scheme for harmonic power sharing in an islanded microgrid," *IEEE Transactions on Power Delivery*, vol. 31, no. 3, pp. 936-945, Jun. 2016.

[11] M. Naderi, Q. Shafiee, F. Blaabjerg *et al.*, "Synchronization stability of interconnected microgrids with fully inverter-based distributed energy resources," *Journal of Modern Power Systems and Clean Energy*, vol. 11, no. 4, pp. 1257-1268, Jul. 2023.

[12] A. Tayyebi, D. Groß, A. Anta *et al.*, "Frequency stability of synchronous machines and grid-forming power converters," *IEEE Journal of Emerging and Selected Topics in Power Electronics*, vol. 8, no. 2, pp. 1004-1018, Jun. 2020.

[13] R. Wang, Q. Sun, Y. Gui *et al.*, "Exponential-function-based droop control for islanded microgrids," *Journal of Modern Power Systems and Clean Energy*, vol. 7, no. 4, pp. 899-912, Jul. 2019.

[14] E. Rokrok, M. Shafie-Khah, and J. P. S. Catalão, "Review of primary voltage and frequency control methods for inverter-based islanded microgrids with distributed generation," *Renewable and Sustainable Energy Reviews*, vol. 82, no. 3, pp. 3225-3235, Feb. 2018.

[15] V. Nasirian, Q. Shafiee, M. J. Guerrero *et al.*, "Droop-free distributed control for AC microgrids," *IEEE Transactions on Power Electronics*, vol. 31, no. 2, pp. 1600-1617, Feb. 2015.

[16] H. Han, Y. Liu, Y. Sun *et al.*, "An improved droop control strategy for reactive power sharing in islanded microgrid," *IEEE Transactions on Power Electronics*, vol. 30, no. 6, pp. 3133-3141, Jun. 2015.

[17] J. Zhou, S. Kim, H. Zhang *et al.*, "Consensus-based distributed control for accurate reactive, harmonic, and imbalance power sharing in microgrids," *IEEE Transactions on Smart Grid*, vol. 9, no. 4, pp. 2453-2467, Jul. 2018.

[18] C. Zhao, E. Mallada, and F. Dörfler, "Distributed frequency control for stability and economic dispatch in power networks," in *Proceedings of 2015 American Control Conference (ACC)*, Chicago, USA, Jul. 2015, pp. 2359-2364.

[19] C. X. Rosero, M. Velasco, P. Martí *et al.*, "Active power sharing and frequency regulation in droop-free control for islanded microgrids under electrical and communication failures," *IEEE Transactions on Industrial Electronics*, vol. 67, no. 8, pp. 6461-6472, Aug. 2020.

[20] S. M. Mohiuddin and J. Qi, "Droop-free distributed control for AC microgrids with precisely regulated voltage variance and admissible voltage profile guarantees," *IEEE Transactions on Smart Grid*, vol. 11, no. 3, pp. 1956-1967, May 2020.

[21] L. Li, H. Ye, Y. Sun *et al.*, "A communication-free economical-sharing scheme for cascaded-type microgrids," *International Journal of Electrical Power & Energy Systems*, vol. 104, pp. 1-9, Jan. 2019.

[22] C. Zhao and S. Low, "Optimal decentralized primary frequency control in power networks," in *Proceedings of 53rd IEEE Conference on Decision and Control*, Los Angeles, USA, Dec. 2014, pp. 2467-2473.

[23] A. J. Babqi and A. H. Etemadi, "MPC-based microgrid control with supplementary fault current limitation and smooth transition mechanisms," *IET Generation, Transmission & Distribution*, vol. 11, no. 9, pp. 2164-2172, Jun. 2017.
[24] C. X. Rosero, M. Gavilánez, and C. Mejía-Echeverría, "Droop-free sliding-mode control for active-power sharing and frequency regulation in inverter-based islanded microgrids," *Energies*, vol. 16, no. 18, pp. 1-14, Aug. 2023.
[25] S. S. Madani, C. Kammer, and A. Karimi, "Data-driven distributed combined primary and secondary control in microgrids," *IEEE Transactions on Control Systems Technology*, vol. 29, no. 3, pp. 1340-1347, May 2021.
[26] Z. Wang, W. Wu, and B. Zhang, "A distributed quasi-newton method for droop-free primary frequency control in autonomous microgrids," *IEEE Transactions on Smart Grid*, vol. 9, no. 3, pp. 2214-2223, May 2018.
[27] J. Moreno-Valenzuela, "A class of proportional-integral with anti-windup controllers for DC-DC buck power converters with saturating input," *IEEE Transactions on Circuits and Systems II: Express Briefs*, vol. 67, no. 1, pp. 157-161, Jan. 2020.
[28] P. Ghignoni, N. Buratti, D. Invernizzi *et al.*, "Anti-windup design for directionality compensation with application to quadrotor UAVs," *IEEE Control Systems Letters*, vol. 5, no. 1, pp. 331-336, Jan. 2021.
[29] H. K. Khalil, *Nonlinear Systems*, 3rd ed., Upper Saddle River: Patience Hall, 2002.
[30] D. Bertsekas, *Dynamic Programming and Optimal Control*, vol. 1, Nashua: Athena Scientific, 2012.
[31] S. Shcherbovskykh, K. Kozlowski, and D. Pazderski, "Evaluation of integral anti-windup feedback coefficient for PI regulator," in *Proceedings of 2018 IEEE 9th International Conference on Dependable Systems, Services and Technologies (DESSERT)*, Kyiv, Ukraine, May 2018, pp. 74-77.
[32] Tesla. (2023, Sept.). Tesla Powerwall 2. [Online]. Available: https://www. tesla. com/sites/default/files/pdfs/powerwall/Powerwall_2_AC_Datasheet_EN_NA.pdf
[33] Renogy. (2023, Sept.). Deep cycle GEL battery. [Online]. Available: https://www. renogy. com/content/RBT200GEL12-G1/GEL200-Datasheet.pdf
[34] W. Jing, C. Lai, D. K. X. Ling *et al.*, "Battery lifetime enhancement via smart hybrid energy storage plug-in module in standalone photovoltaic power system," *Journal of Energy Storag*e, vol. 11, pp. 586-598, Feb. 2019.
[35] SolarEdge. (2023, Sept.). SolarEdge storage solution. [Online]. Available: https://www. solaredge. com/sites/default/files/single_phase_storedge_solutions_datasheet_na.pdf
[36] J. M. Guerrero, J. C. Vasquez, J. Matas *et al.*, "Hierarchical control of droop-controlled AC and DC microgrids – a general approach toward standardization," *IEEE Transactions on Industrial Electronics*, vol. 58, no. 1, pp. 158-172, Jan. 2011.
[37] M. Parvania and R. Khatami, "Continuous-time marginal pricing of electricity," *IEEE Transactions on Power Systems*, vol. 32, no. 3, pp. 1960-1969, May 2017.
[38] J. Yan, M. Menghwar, E. Asghar *et al.*, "Real-time energy management for a smart-community microgrid with battery swapping and renewables," *Applied Energy*, vol. 238, pp. 180-194, Mar. 2019.
[39] W. Liu, U. Prasad, L. Wu *et al.*, "Stability analysis on normalized active power consensus-based droop-free control schemes in islanded AC microgrid," *IEEE Transactions on Smart Grid*, 2024 (under review).
[40] K. Zuo and L. Wu, "Eigenvalue-based stability analysis for droop-free controlled islanded microgrid with symmetric/asymmetric communication network," *IEEE Transactions on Smart Grid*, vol. 13, no. 4, pp. 2511-2522, Jul. 2022.
[41] R. C. Dugan and W. H. Kersting, "Induction machine test case for the 34-bus test feeder description," in *Proceedings of 2006 IEEE PES General Meeting*, Montreal, Canada, Jun. 2006, pp. 1-4.
[42] R. Leng, Z. Li, and Y. Xu, "Two-stage stochastic programming for coordinated operation of distributed energy resources in unbalanced active distribution networks with diverse correlated uncertainties," *Journal of Modern Power Systems and Clean Energy*, vol. 11, no. 1, pp. 120-131, Jan. 2023.
[43] Q. Shafiee, J. M. Guerrero, and J. C. Vasquez, "Distributed secondary control for islanded microgrids – a novel approach," *IEEE Transactions on Power Electronics*, vol. 29, no. 2, pp. 1018-1031, Feb. 2014.
[44] Y. Zhang, M. Hong, E. Dall'Anese *et al.*, "Distributed controllers seeking AC optimal power flow solutions using ADMM," *IEEE Transactions on Smart Grid*, vol. 9, no. 5, pp. 4525-4537, Sept. 2018.
[45] M. Dokus and A. Mertens, "On the coupling of power-related and inner inverter control loops of grid-forming converter systems," *IEEE Access*, vol. 9, pp. 16173-16192, Jan. 2021.
[46] K. P. Schneider, J. C. Fuller, and D. P. Chassin, "Multi-state load models for distribution system analysis," *IEEE Transactions on Power System*, vol. 26, no. 4, pp. 2425-2433, Nov. 2011.
[47] Y. Chen, R. Leonard, M. Keyser *et al.*, "Development of performance-based two-part regulating reserve compensation on MISO energy and ancillary service market," *IEEE Transactions on Power Systems*, vol. 30, no. 1, pp. 142-155, Jan. 2015.
[48] N. Soni, S. Doolla, and M. C. Chandorkar, "Improvement of transient response in microgrids using virtual inertia," *IEEE Transactions on Power Delivery*, vol. 28, no. 3, pp. 1830-1838, Jul. 2013.

Kunyu Zuo received the B.S. and M.S. degrees in electrical engineering from Sichuan University, Chengdu, China, in 2016 and 2019, respectively. From 2017 to 2018, he was a Visiting Student at School of Electronics, Electrical Engineering and Computer Science, Queen's University Belfast, UK. He is currently pursuing the Ph.D. degree in the Electrical and Computer Engineering Department, Stevens Institute of Technology, Hoboken, USA. His research interests include renewable microgrid solutions and distributed control.

Lei Wu received the B.S. degree in electrical engineering and the M.S. degree in systems engineering from Xi'an Jiaotong University, Xi'an, China, in 2001 and 2004, respectively, and the Ph.D. degree in electrical engineering from Illinois Institute of Technology (IIT), Chicago, USA, in 2008. From 2008 to 2010, he was a Senior Research Associate with the Robert W. Galvin Center for Electricity Innovation, IIT. He was a summer Visiting Faculty at NYISO in 2012. He was a Professor with the Electrical and Computer Engineering Department, Clarkson University, Potsdam, USA, till 2018. He is currently the Anson Wood Burchard Chair Professor with the Electrical and Computer Engineering Department, Stevens Institute of Technology, Hoboken, USA. His research interests include power systems operation and planning, energy economics, and community resilience microgrid.